nature medicine

# Modeling the mitochondrial cardiomyopathy of Barth syndrome with induced pluripotent stem cell and heart-on-chip technologies

Gang Wang[1,14], Megan L McCain[2,14], Luhan Yang[2,3], Aibin He[1], Francesco Silvio Pasqualini[2], Ashutosh Agarwal[2], Hongyan Yuan[2], Dawei Jiang[1], Donghui Zhang[1], Lior Zangi[1], Judith Geva[1], Amy E Roberts[1,4], Qing Ma[1], Jian Ding[1], Jinghai Chen[1], Da-Zhi Wang[1], Kai Li[1], Jiwu Wang[5,6], Ronald J A Wanders[7], Wim Kulik[7], Frédéric M Vaz[7], Michael A Laflamme[8], Charles E Murry[8–10], Kenneth R Chien[11], Richard I Kelley[12], George M Church[2,3], Kevin Kit Parker[2,13] & William T Pu[1,13]

**Study of monogenic mitochondrial cardiomyopathies may yield insights into mitochondrial roles in cardiac development and disease. Here, we combined patient-derived and genetically engineered induced pluripotent stem cells (iPSCs) with tissue engineering to elucidate the pathophysiology underlying the cardiomyopathy of Barth syndrome (BTHS), a mitochondrial disorder caused by mutation of the gene encoding tafazzin (*TAZ*). Using BTHS iPSC-derived cardiomyocytes (iPSC-CMs), we defined metabolic, structural and functional abnormalities associated with *TAZ* mutation. BTHS iPSC-CMs assembled sparse and irregular sarcomeres, and engineered BTHS 'heart-on-chip' tissues contracted weakly. Gene replacement and genome editing demonstrated that *TAZ* mutation is necessary and sufficient for these phenotypes. Sarcomere assembly and myocardial contraction abnormalities occurred in the context of normal whole-cell ATP levels. Excess levels of reactive oxygen species mechanistically linked *TAZ* mutation to impaired cardiomyocyte function. Our study provides new insights into the pathogenesis of Barth syndrome, suggests new treatment strategies and advances iPSC-based *in vitro* modeling of cardiomyopathy.**



BTHS is an X-linked cardiac and skeletal mitochondrial myopathy caused by mutation of the gene encoding tafazzin[1], an acyltransferase responsible for normal acylation of cardiolipin, the major phospholipid of the mitochondrial inner membrane[2] (**Supplementary Fig. 1**; data tables for supplementary data are available as **Supplementary Data Sets**). Cardiolipin abnormalities also occur in ischemic heart disease and aging and have been implicated in the cardiac dysfunction characteristic of these conditions[3]. The mechanisms that lead from abnormal cardiolipin biogenesis to cardiomyopathy are not well understood. Here, we combined patient-derived iPSCs, genome editing, modified RNA (modRNA)[4] and bioengineered microchips that simulate myocardial tissue ('heart-on-chip')[5] to replicate the pathophysiology of BTHS cardiomyopathy in tissue constructs. Using these approaches, we identified mitochondrial functional abnormalities caused by *TAZ* mutation and cardiolipin deficiency. We show that *TAZ* mutation is necessary and sufficient to disrupt sarcomere assembly and contractile stress generation and that these functional abnormalities are not due to global ATP depletion. Furthermore, we show that the BTHS cardiomyopathic phenotype is readily reversed by re-introduction of wild-type (WT) TAZ or by suppression of excessive reactive oxygen species (ROS) produced by BTHS mitochondria. These results provide new insights into the links between mitochondrial function, sarcomere assembly and muscle contractile activity and suggest new therapeutic strategies for BTHS.

## RESULTS

### An iPSC-CM model of BTHS

To investigate BTHS pathogenesis in a controlled *in vitro* setting, we generated iPSCs from two unrelated individuals with BTHS. Two iPSC lines, BTH-H and BTH-C, reprogrammed using retroviral[6] or modRNA approaches[7,8], respectively, had confirmed *TAZ* frameshift (c.517delG) and missense (c.328T>C) mutations, respectively.

[1]Department of Cardiology, Boston Children's Hospital, Boston, Massachusetts, USA. [2]Wyss Institute for Biologically Inspired Engineering, School of Engineering and Applied Sciences, Harvard University, Cambridge, Massachusetts, USA. [3]Department of Genetics, Harvard Medical School, Boston, Massachusetts, USA. [4]Department of Medicine, Division of Genetics, Boston Children's Hospital, Boston, Massachusetts, USA. [5]Allele Biotechnology & Pharmaceuticals, Inc., San Diego, California, USA. [6]Department of Photobiology and Bioengineering, The Scintillon Institute, San Diego, California, USA. [7]Department of Clinical Chemistry and Pediatrics, Laboratory of Genetic Metabolic Diseases, Academic Medical Center, Amsterdam, The Netherlands. [8]Department of Pathology, Center for Cardiovascular Biology and Institute for Stem Cell and Regenerative Medicine, University of Washington, Seattle, Washington, USA. [9]Department of Bioengineering, Center for Cardiovascular Biology, Institute for Stem Cell and Regenerative Medicine, University of Washington, Seattle, Washington, USA. [10]Department of Medicine and Cardiology, Center for Cardiovascular Biology, Institute for Stem Cell and Regenerative Medicine, University of Washington, Seattle, Washington, USA. [11]Department of Cell and Molecular Biology and Medicine, Karolinska Institutet, Stockholm, Sweden. [12]Division of Metabolism, Kennedy Krieger Institute, Baltimore, Maryland, USA. [13]Harvard Stem Cell Institute, Harvard University, Cambridge, Massachusetts, USA. [14]These authors contributed equally to this work. Correspondence should be addressed to W.T.P. (wpu@enders.tch.harvard.edu) or K.K.P. (kkparker@seas.harvard.edu).

Received 22 August 2013; accepted 24 March 2014; published online 11 May 2014; doi:10.1038/nm.3545

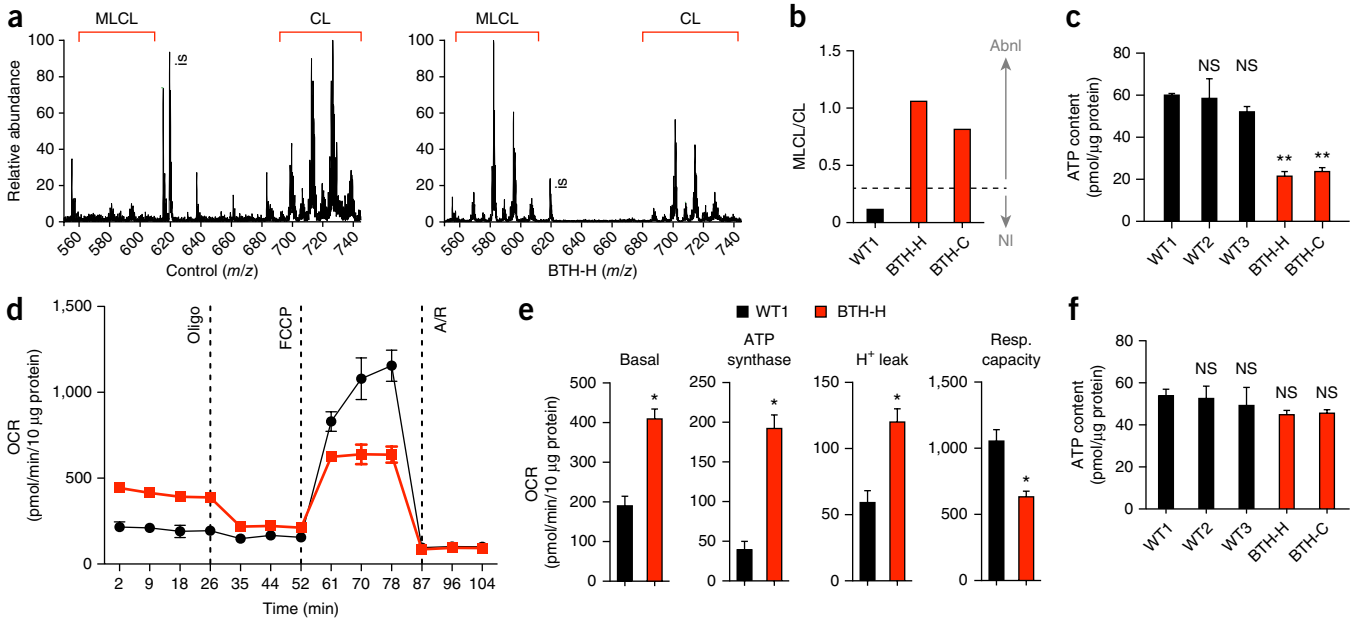


**Figure 1** Mitochondrial abnormalities in BTHS iPSC-CMs. (**a**) Mass spectroscopy analysis of control and BTH-H phospholipids showing mature cardiolipin (CL) and immature cardiolipin (monolysocardiolipin, MLCL) content of BTHS versus control iPSC-CMs. is, internal standard. (**b**) The MLCL/CL ratio in BTH-H, BTH-C and control iPSC-CMs. The dashed line indicates the clinical diagnostic threshold for BTHS. $n = 2$. AbnI, abnormal; NI, normal. (**c**) ATP levels in BTHS and control iPSC-CMs cultured in galactose. $n = 3$. $^{**}P < 0.01$, Student's *t*-test. NS, not significant. (**d**,**e**) Mitochondrial function of BTH-H and control (WT1) iPSC-CMs in galactose culture, as assessed by the cellular oxygen consumption rate (OCR), normalized to total protein. The OCR measurements are defined in **Supplementary Figure 5b**,**c**. Shown are representative time course data (**d**) and aggregate data (**e**) for $n = 3$ independent experiments. $^{*}P < 0.05$, Student's *t*-test. Oligo, oligomycin; FCCP, carbonyl cyanide-4-(trifluoromethoxy)phenylhydrazone; A/R, antimycin plus rotenone; Resp., respiratory. (**f**) ATP levels in BTHS (BTH-H and BTH-C) and control iPSC-CMs (WT1, WT2 and WT3) cultured in glucose. $n = 3$. Data are expressed as mean ± s.e.m.

These iPSC lines had normal karyotype and met pluripotency criteria (**Supplementary Fig. 2**; all cell lines in this study are summarized in **Supplementary Table 1**). As controls, we used three normal iPSC lines, generated by retroviral (WT1 and WT2) or modRNA (WT3) reprogramming (**Supplementary Table 1**). We carried out the experiments presented below multiple times and using multiple cell lines with consistent results; we provide representative data in the accompanying figures and supplementary information and an overview of the data collected in **Supplementary Table 2**.

We differentiated the iPSCs into iPSC-CMs using an established protocol[9] (**Supplementary Fig. 3a–c**), and then used magnetic cell sorting for the cardiomyocyte surface marker vascular cell adhesion molecule-1 (VCAM-1)[10,11] to obtain preparations containing ~80% iPSC-CMs (**Supplementary Fig. 3d–f**). On replating, the enriched myocytes formed sheets of cardiomyocytes (**Supplementary Fig. 3g**) that beat spontaneously (**Supplementary Movie 1**).

BTHS is characterized by depletion of mature cardiolipin and accumulation of an immature form, monolysocardiolipin (**Supplementary Fig. 1**)[12,13]. Phospholipid profiles of BTHS iPSC-CMs, measured by mass spectrometry, confirmed that abnormal cardiolipin processing was recapitulated in BTHS iPSC-CMs (**Fig. 1a**). The monolysocardiolipin-to-cardiolipin ratio in BTHS iPSC-CMs exceeded 0.3, the clinically used diagnostic threshold for BTHS[13] (**Fig. 1a**,**b**). Thus, BTHS iPSC-CMs exhibited impaired cardiolipin biogenesis that matched what is observed clinically in patients with BTHS.

We assessed mitochondrial morphology and function in BTHS iPSC-CMs. FACS analysis showed that BTHS iPSC-CMs had mitochondrial numbers similar to those of control iPSC-CMs and that BTHS iPSC-CM mitochondria were smaller than control mitochondria (**Supplementary Fig. 4a**,**b**). This smaller size was associated with greater fragmentation of BTHS iPSC-CM mitochondria compared to the more highly networked mitochondria of controls (**Supplementary Fig. 4c**). To assess BTHS mitochondrial function, we cultured iPSC-CMs in galactose-based medium, which has limited ability to support ATP production via glycolysis[14]. Under these conditions, BTHS iPSC-CM ATP levels were significantly lower than those of wild-type iPSC-CMs (**Fig. 1c**). Consistent with cellular energy deprivation, the activated form of AMP-dependent kinase was markedly upregulated in BTHS iPSC-CMs (**Supplementary Fig. 5a**). Next, we used an extracellular flux analyzer to probe mitochondrial function (the approach and the terms used are described in **Supplementary Fig. 5b**,**c**). BTHS iPSC-CMs unexpectedly exhibited an elevated basal oxygen consumption rate, which was a result of both increased $F_1F_0$ ATP synthase oxygen consumption and increased '$H^+$ leak' (**Fig. 1d**,**e** and **Supplementary Fig. 5d**). In the context of reduced basal ATP levels, these data pointed to inefficient $F_1F_0$ ATP synthase activity, which we confirmed by selective complex immunocapture followed by measurement of $F_1F_0$ ATP synthase quantity and activity (**Supplementary Fig. 5e**). We also measured respiratory capacity, which reflects maximal electron transport chain activity, and found that it was severely impaired in BTHS iPSC-CMs (**Fig. 1d**,**e**). Collectively, these data demonstrate that TAZ deficiency and consequent cardiolipin abnormalities reduce peak electron transport chain function and decrease ATP generation efficiency by lowering $F_1F_0$ ATP synthase–specific activity. The metabolic abnormalities of BTHS iPSC-CMs were not evident in BTHS primary fibroblasts or iPSCs (**Supplementary Fig. 5f**,**g**), consistent with the muscle-selective phenotype of patients with BTHS.

Cardiomyocytes are capable of producing ATP through both glycolysis and oxidative phosphorylation. We hypothesized that glucose, an

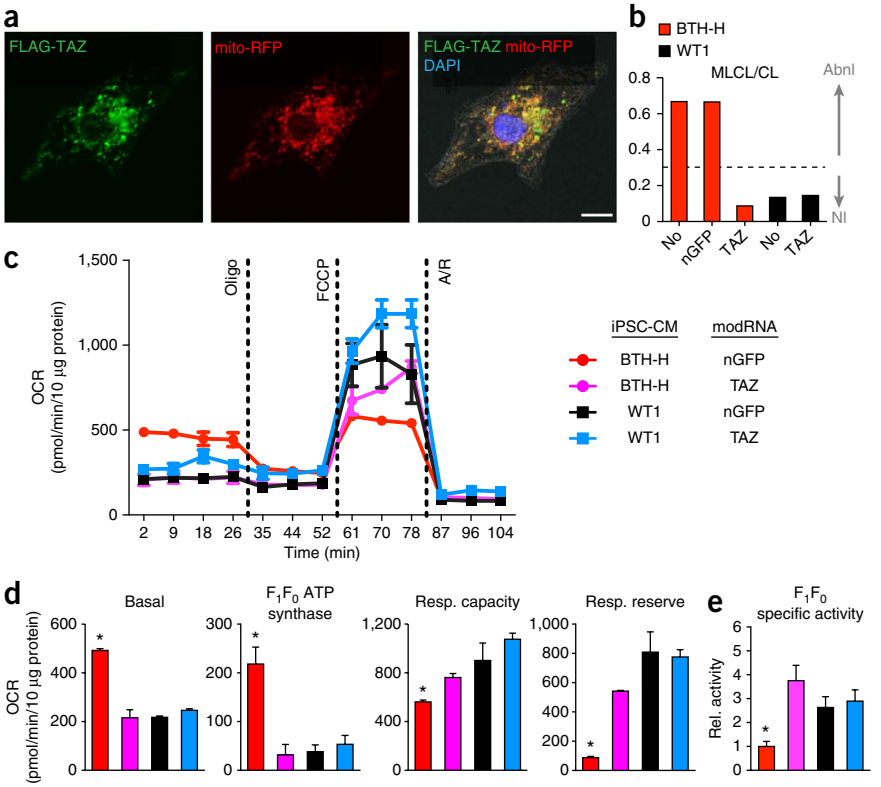


**Figure 2** TAZ deficiency is necessary to cause the iPSC-CM metabolic phenotype. (**a**) Subcellular localization of Flag-tagged TAZ, delivered to control (WT1) iPSC-CMs by modRNA transfection. Localization to mitochondria was assessed by co-localization with virally delivered RFP targeted to mitochondria (mito-RFP). Scale bar, 10 µm. (**b**) Cardiolipin maturation as determined by phospholipid mass spectroscopy in BTH-H or control (WT1) iPSC-CMs without transfection (No) or transfected with nuclear-localized GFP (nGFP) or *TAZ* modRNA. An MLCL/CL ratio below 0.3 (dashed line) is considered normal. (**c**,**d**) Mitochondrial function in BTH-H and control (WT1) iPSC-CMs transfected with the indicated modRNAs, as assessed by the cellular OCR, normalized to total protein. The OCR measurements are defined in **Supplementary Figure 5b**,**c**. Shown are representative time course data (**c**) and aggregate data (**d**) for $n = 3$ independent experiments. $^*P < 0.05$, Student's *t*-test. (**e**) $F_1F_0$ ATP synthase specific activity, as measured by selective complex immunocapture. $n = 6$. $^*P < 0.05$, Student's *t*-test. Data are expressed as mean ± s.e.m.

energy source that supports both glycolysis and oxidative phosphorylation, would normalize ATP levels. Indeed, glucose induced glycolysis and triggered a metabolic shift away from oxidative phosphorylation in both BTHS and control iPSC-CMs (**Supplementary Fig. 5h**,**i**). This metabolic shift normalized BTHS iPSC-CM ATP levels and basal oxygen consumption rate (**Fig. 1f** and **Supplementary Fig. 5j**). However, glucose culture did not correct the markedly depressed respiratory capacity of BTHS iPSC-CMs (**Supplementary Fig. 5j**). These observations indicate that glucose restores basal ATP levels through increased glycolysis but does not correct underlying mitochondrial defects in the electron transport chain.

### *TAZ* mutation causes BTHS iPSC-CM phenotypes

Because iPSCs derived from patients with BTHS and control iPSCs have numerous genetic differences other than *TAZ* mutation, we took three independent approaches to further establish the causative role of *TAZ* mutation in abnormal cardiolipin biogenesis and mitochondrial function. First, we used adenoviral delivery of *TAZ*-specific short hairpin RNAs (shRNAs) to deplete *TAZ* in neonatal rat ventricular cardiomyocytes (NRVMs) by over 80% at 72 h after infection (**Supplementary Fig. 6a**). At this time point, cardiolipin profiles in NRVMs with *TAZ* knockdown were already highly abnormal (**Supplementary Fig. 6b**), indicating rapid turnover of TAZ and mature cardiolipin. As in BTHS iPSC-CMs, *TAZ* deficiency in NRVMs grown in galactose reduced ATP levels, activated AMP-dependent kinase (**Supplementary Fig. 6c**,**d**) and caused comparable abnormalities in mitochondrial function (**Supplementary Fig. 6e**). Electron microscopy did not reveal alterations in mitochondrial morphology or number in this short-term *TAZ* depletion experiment (**Supplementary Fig. 6f**), suggesting that mitochondrial functional abnormalities are not contingent upon the mitochondrial structural abnormalities observed in patients with BTHS.

Second, we used modRNA technology[4,7,15] in which 5-methylcytidine and pseudouridine are substituted for cytidine and pseudouridine, respectively, to efficiently re-introduce *TAZ* into BTHS iPSC-CMs. Cardiomyocytes, including iPSC-CMs, are refractory to standard transfection methods. modRNA has minimal toxicity[4,7,15] and efficiently transfects cardiomyocytes[16] (**Supplementary Fig. 7**). *TAZ* modRNA likewise transfected iPSC-CMs, and TAZ protein localized to mitochondria (**Fig. 2a**). *TAZ* modRNA restored cardiolipin biogenesis and normalized basal mitochondrial function in BTHS iPSC-CMs, although maximal respiratory capacity was rescued incompletely (**Fig. 2b–e**). These results indicate that *TAZ* mutation is necessary to confer the BTHS mitochondrial phenotype and that this phenotype is rapidly reversed upon TAZ restoration.

Third, we used Cas9-mediated scarless genome editing[17] to mutate *TAZ* in the control human iPSC line PGP1-iPSC, yielding three iPSC lines that are isogenic except for the sequence of *TAZ* exon 6 (**Supplementary Table 1** and **Fig. 3a–c**; the Online Methods and **Supplementary Fig. 8** contain details on the construction and validation of these iPSC lines). PGP1-TAZ$^{c.517delG}$ contains the *TAZ* frameshift mutation from the BTH-H line (1-nt deletion), and PGP1-TAZ$^{c.517ins}$ contains a distinct frameshift mutation at the same site (14-nt insertion; **Fig. 3a–c**). PGP1-TAZ$^{WT}$ is a control line that was handled identically to the PGP1-TAZ$^{c.517delG}$ and PGP1-TAZ$^{c.517ins}$ lines but contains a WT *TAZ* sequence. iPSC-CMs derived from these isogenic *TAZ* mutant lines fully recapitulated the cardiolipin, mitochondrial and ATP deficits that we observed in patient-derived iPSC and NRVM *TAZ* knockdown models (**Fig. 3d–g** and **Supplementary Table 2**). Together, these data indicate that *TAZ* mutation alone is sufficient to cause these defects in an otherwise unaffected genetic background.

### Abnormal sarcomerogenesis in BTHS iPSC-CMs

Mitochondria regulate cardiomyocyte maturation[18], a hallmark of which is assembly of organized arrays of sarcomeres. We noticed that BTH-H iPSC-CMs grown on an unpatterned gelatin substrate assembled sarcomeres more irregularly than did control iPSC-CMs. To compare sarcomere architecture more precisely, we engineered

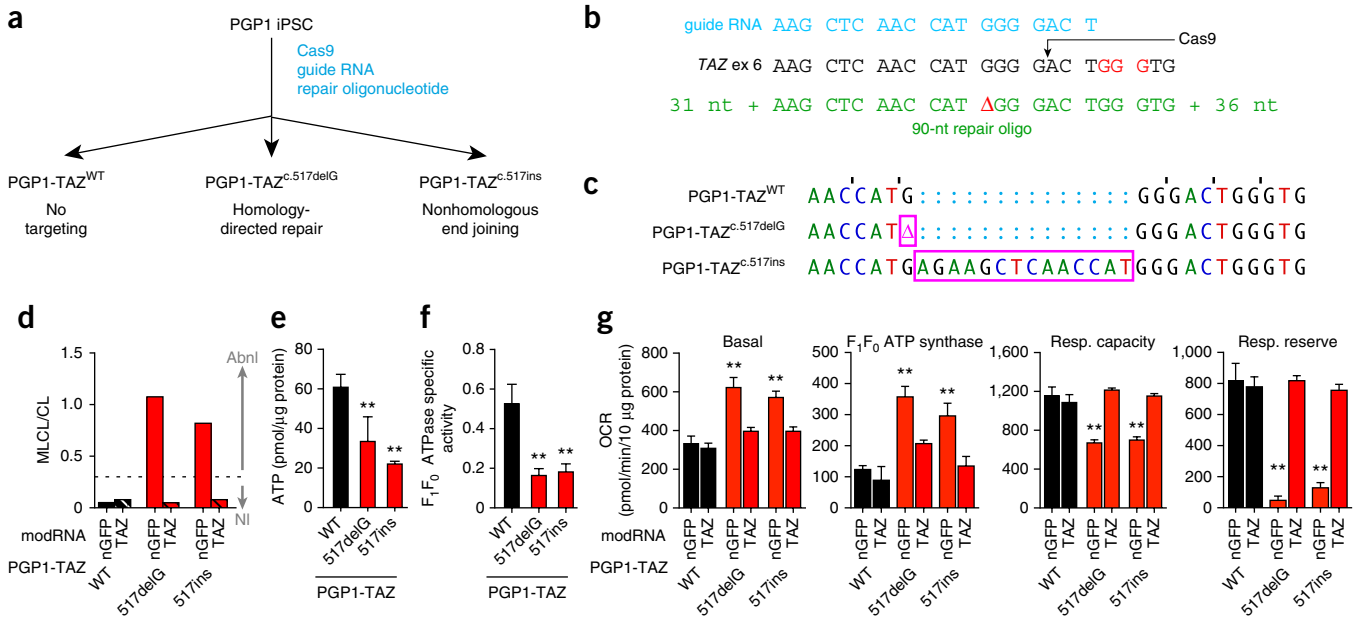


**Figure 3** Construction and characterization of *TAZ* mutant and isogenic control iPSCs by Cas9-mediated genome editing. (**a**) Schematic of genome editing strategy. (**b**) Strategy for modification of *TAZ* exon 6 (ex 6) using Cas9, the indicated guide RNA and the indicated repair oligonucleotide. (**c**) Sequence of a region of *TAZ* exon 6 in genome-edited cell lines. Purple boxes indicate deletion (Δ) or insertion. PGP1-TAZ$^{WT}$ was not modified and had WT *TAZ* sequence, PGP1-TAZ$^{c.517delG}$ contained the BTH-H mutation and PGP1-TAZ$^{c.517ins}$ contained the indicated insertion. (**d**) Phospholipid mass spectroscopy assessment of cardiolipin maturation in *TAZ* mutant and isogenic control (WT) iPSC-CMs transfected with nuclear-localized GFP (nGFP) or *TAZ* modRNA. (**e**) Basal ATP levels in *TAZ* mutant and isogenic control iPSC-CMs cultured in galactose medium. $^{**}P < 0.01$, *t*-test. $n = 3$. (**f**) $F_1F_0$ ATPase specific activity in *TAZ* mutant and isogenic control iPSC-CMs. $^{**}P < 0.01$, Student's *t*-test. $n = 3$. (**g**) Mitochondrial function in *TAZ* mutant and isogenic control iPSC-CMs transfected with the indicated modRNA, as measured by cellular oxygen consumption rate (**Supplementary Fig. 5b**,**c**). $n = 3$. $^{**}P < 0.01$ by one-way analysis of variance (ANOVA) with Dunnett's *post hoc* test compared to PGP1-TAZ$^{WT}$ + nGFP. Data are expressed as mean ± s.e.m.

iPSC-CM shape by seeding the cells on micropatterned fibronectin rectangles designed to mimic the dimensions of human adult cardiomyocytes[19], with length/width ratios of approximately 7:1 (95 µm × 13 µm). To quantify the global regularity of sarcomere arrangement, we developed an unbiased metric to score images of patterned iPSC-CMs immunostained for the sarcomere protein α-actinin. This metric, which we named sarcomere organization, is based on the regularity of sarcomere spacing, as determined from two-dimensional (2D) Fourier spectra of the sarcomere immunostains (**Supplementary Fig. 9a–c** and Online Methods). Whereas sarcomeres in control iPSC-CMs extended serially along the entire length of the cell, sarcomeres in BTH-H iPSC-CMs were intermittent and sparse (**Fig. 4a**). Treatment with *TAZ* modRNA restored sarcomere regularity (**Fig. 4a**). These differences were reflected in the sarcomere organization metric, which was lower in BTH-H iPSC-CMs than in controls and was increased by *TAZ* modRNA treatment (**Fig. 4a**). Although glucose culture normalized ATP levels to a degree comparable to that achieved with *TAZ* modRNA, glucose culture did not rescue sarcomere formation (**Fig. 4a**). These defects in sarcomere assembly were recapitulated in genome-edited PGP1-TAZ$^{c.517delG}$ and PGP1-TAZ$^{c.517ins}$ iPSC-CMs but were not observed in isogenic PGP1-TAZ$^{WT}$ controls (**Fig. 4b**), confirming the causative role of the BTH-H exon 6 frameshift *TAZ* mutation. These data suggest that sarcomerogenesis is sensitive to mitochondrial function independently of whole-cell ATP levels.

Notably, BTH-C iPSC-CMs exhibited sarcomere organization that was not significantly different from that of controls (**Fig. 4c**). This phenotypic heterogeneity between BTH-H and BTH-C iPSC-CMs may be due to the nature of the specific *TAZ* mutations or to other variables between the cell lines. Further use of genome-edited cell lines will be necessary to better understand genotype-phenotype relationships in this disease.

### Heart-on-chip model of BTHS myopathy and its genetic rescue

Because patients with BTHS often develop cardiomyopathy, we asked whether we could replicate the contractile pathophysiology of BTHS in an *in vitro* model of engineered myocardium and demonstrate the efficacy of *TAZ* modRNA treatment in this model. Toward this goal, we used our heart-on-chip assay[5,20] to quantitatively measure the contractility of engineered myocardial tissue assembled from BTHS or control iPSC-CMs. iPSC-CMs selected via magnetic-activated cell sorting (MACS) were seeded onto thin elastomers micropatterned with fibronectin lines and supported by glass coverslips[21,22]. Over a 5-d culture period, the iPSC-CMs self-organized into laminar anisotropic myocardium. Staining for sarcomeric α-actinin in control iPSC-CM–containing tissue revealed both aligned sarcomeres and fibrous structures indicative of the relatively immature phenotype of iPSC-CMs (**Fig. 5a**), findings that are similar to previous observations in immature primary rat cardiac myocytes[23]. Like individual iPSC-CMs seeded on fibronectin rectangles, engineered BTHS iPSC-CM–containing tissue exhibited impaired sarcomere assembly compared to controls (**Supplementary Fig. 10a**). We then peeled precut muscular thin film (MTF) tissue constructs from the glass substrate, allowing them to contract and curl away from the plane of the coverslip (**Fig. 5a** and **Supplementary Movie 2**). We used movies of contracting MTFs to calculate radii of curvature, from which we calculated the diastolic and peak systolic stresses using a modification of Stoney's equation[5,21,24]. Twitch stress was calculated as the difference

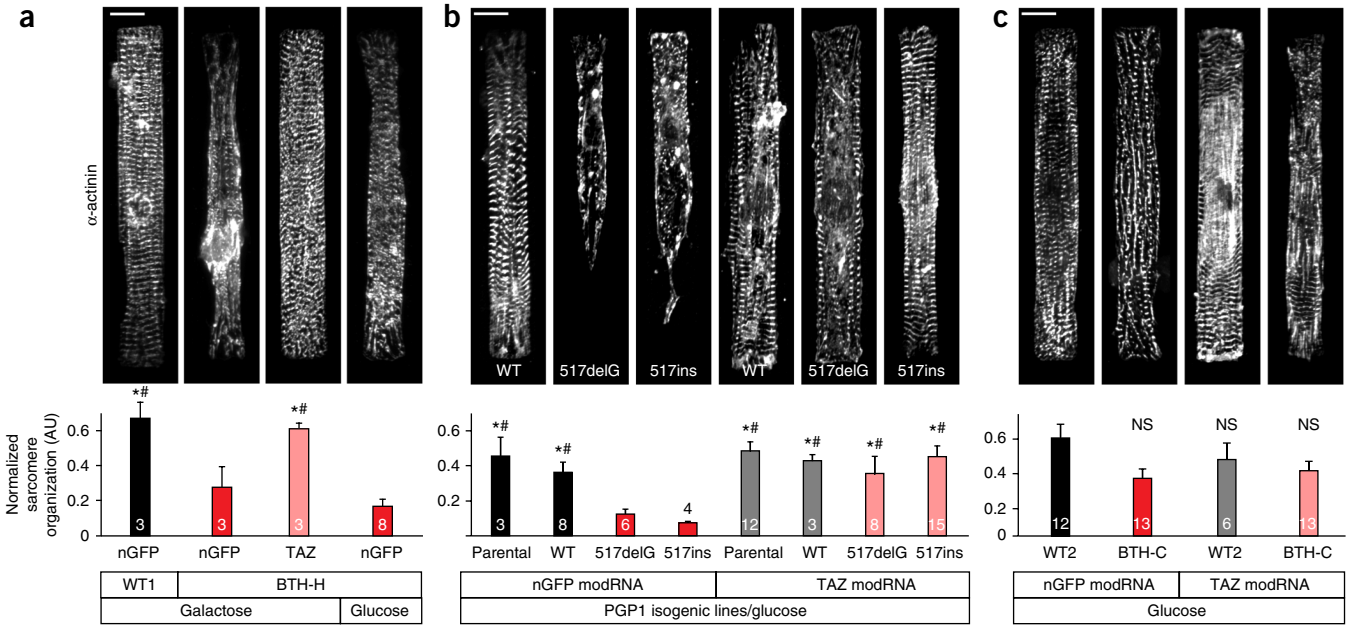


**Figure 4** Sarcomere organization is impaired in BTH-H mutant iPSC-CMs. Representative images show α-actinin staining of iPSC-CMs seeded on micropatterned fibronectin rectangles with length/width ratios of 7:1 (95 μm × 13 μm). Plots show quantitative assessment of sarcomere organization using an unbiased 2D Fourier transform–based algorithm (Online Methods). (**a**) Sarcomere organization of BTH-H and control (WT1) iPSC-CMs, as assessed in the indicated culture medium after transfection with the indicated modRNA. $P < 0.05$ versus BTH-H + nGFP, galactose (*) or BTH-H + nGFP, glucose (#). (**b**) Sarcomere organization of genome-edited, isogenic PGP1 iPSC-CMs containing the indicated TAZ variant in glucose medium. iPSC-CMs were transfected with the indicated modRNA. $P < 0.05$ versus PGP1-TAZ$^{c.517delG}$ + nGFP (*) or PGP1-TAZ$^{c.517ins}$ + nGFP (#). (**c**) Sarcomere organization of BTH-C and control (WT2) iPSC-CMs after transfection with the indicated modRNA in glucose medium. Statistical comparisons by ANOVA with Fisher's least-significant difference *post hoc* test. Sample number (*n*) is indicated by the number within each the bar. Scale bars, 10 μm. Data are expressed as mean ± s.e.m.

between diastolic and peak systolic stress (**Fig. 5a**). During electrical field stimulation, control iPSC-CM MTFs contracted rhythmically at frequencies ranging from 1 to 5 Hz (**Fig. 5b**, **Supplementary Fig. 10b** and **Supplementary Movie 2**). BTH-H iPSC-CM tissues developed significantly lower twitch and peak systolic stress compared to controls over the same stimulation frequency range, indicating that BTHS engineered myocardial tissue recapitulates the BTHS myopathic phenotype.

Next, we asked whether these engineered myocardial tissue constructs effectively model disease correction. Treatment of BTH-H iPSC-CMs (**Fig. 5b**, **Supplementary Fig. 10** and **Supplementary Movie 2**) with *TAZ* modRNA for 5 d restored contractile function of MTF tissue constructs to levels comparable to those of controls, further confirming that this myopathic phenotype is reversible and due to *TAZ* mutation.

We assessed the contribution of whole-cell ATP to BTHS contractile dysfunction by culturing engineered iPSC-CM MTF constructs in glucose-containing medium, which we showed above increases ATP in BTHS iPSC-CMs to a level comparable to that seen with *TAZ* modRNA treatment. In contrast to *TAZ* modRNA rescue, glucose culture alone did not restore BTH-H iPSC-CM MTF force generation at any tested stimulation frequency (**Fig. 5b**, **Supplementary Fig. 10b**,**c** and **Supplementary Movie 3**). Although local pools of mitochondrially produced ATP might theoretically be required for iPSC-CM force generation, such a mechanism is unlikely because inhibition of mitochondrial ATP production with oligomycin in control iPSC-CM MTFs did not alter their contractile strength (**Supplementary Fig. 11**); this finding is consistent with the immature and highly glycolytic properties of iPSC-CMs. Together, these data show that BTH-H iPSC-CMs have a severe defect in contractility that occurs independently of ATP depletion. This result is consistent with anectodal data we obtained from a patient with BTHS that showed preserved cardiac high-energy phosphate levels in the setting of impaired heart function (**Supplementary Fig. 12**). Taken together, these data suggest that contractile dysfunction in BTHS occurs despite normal myocardial energy stores.

We next reproduced the findings from patient-derived BTHS iPSC-CMs in the isogenic, genome-edited cells. Contractile function of mock-manipulated PGP1-TAZ$^{WT}$ iPSC-CM myocardial constructs was equivalent to that of constructs derived from the parental PGP1 cell line, whereas constructs derived from *TAZ* mutation-containing iPSC-CMs (PGP1- TAZ$^{c.517delG}$ or PGP1- TAZ$^{c.517ins}$) caused severe loss of contractile stress generation (**Fig. 5c**, **Supplementary Fig. 10c** and **Supplementary Movie 4**). Re-introduction of *TAZ* by modRNA restored contractility to mutant tissue constructs (**Fig. 5c**, **Supplementary Fig. 10c** and **Supplementary Movie 4**). Thus, in both patient-derived cells and cells with an isogenic background, TAZ deficiency causes contractile dysfunction.

BTH-C myocardial tissue constructs also showed poor contractile function, which was reflected in their markedly reduced beating activity (**Supplementary Movie 2**) and severely depressed twitch stress (**Fig. 5d**). Systolic stress generation was also reduced significantly in BTH-C myocardial tissue constructs compared to controls (**Fig. 5d**). However, their peak systolic (and diastolic) stresses were substantially higher than in their BTH-H counterparts (**Fig. 5b**,**d**), perhaps reflecting the difference in sarcomere assembly that we observed between these *TAZ* genotypes (**Fig. 4a**,**c**).

### Assessment of potential therapies using BTHS iPSC-CMs

We used BTHS iPSC-CMs to measure the effect of three proposed interventions for BTHS: bromoenol lactone, an inhibitor of

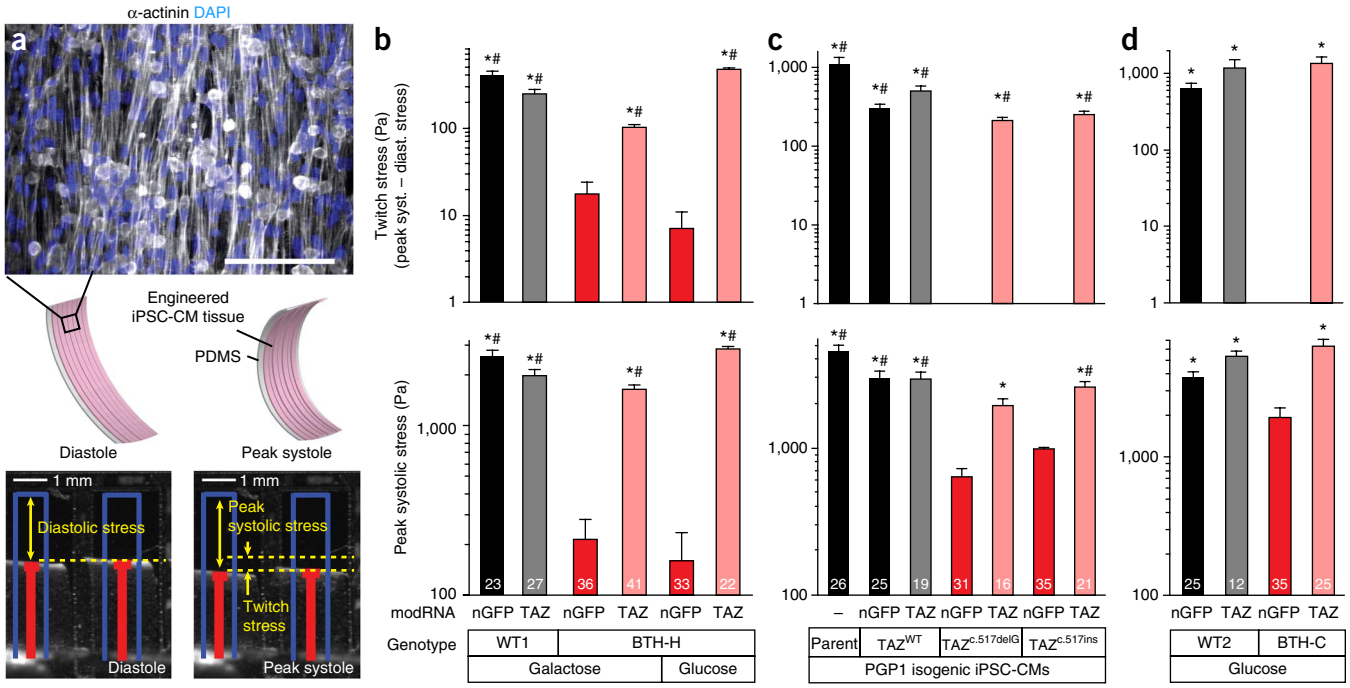


**Figure 5** BTHS myocardial tissue constructs exhibit depressed contractile stress generation. (**a**) Top, α-actinin–stained image of an MTF. Middle, iPSC-CMs seeded onto thin elastomers with patterned lines of fibronectin self-organized into anisotropic myocardial tissues. Cardiomyocyte stress generation reduces the radius of curvature of the construct as it contracts from diastole to peak systole. Scale bar, 100 μm. Bottom, still images of MTFs in diastole and systole. Red lines indicate automated MTF tracking projected onto the horizontal plane. Blue lines indicate lengths of MTFs before peeling from substrate. PDMS, polydimethylsiloxane. (**b**–**d**) Twitch stress and peak systolic (syst.) stress generated by MTFs paced at 2 Hz. MTFs were generated from BTH-H and control (WT1) iPSC-CMs transfected with the indicated modRNA in galactose or glucose culture medium (**b**), genome-edited *TAZ* frameshift and control iPSC-CMs and transfected with the indicated modRNA in glucose culture medium (**c**), and BTH-C and control (WT2) iPSCs transfected with the indicated modRNA in glucose culture medium (**d**). For **b**, $P < 0.05$ versus BTH-H + nGFP, galactose (*) or BTH-H + nGFP + glucose (#). For **c**, $P < 0.05$ versus PGP1-TAZ$^{c.517delG}$ + nGFP (*) or PGP1-TAZ$^{c.517ins}$ + nGFP (#). For **d**, $^*P < 0.05$ versus BTH-C + nGFP. Statistical comparisons by Kruskal-Wallis one-way ANOVA on ranks and Dunn's *post hoc* test. Number of samples (*n*) is indicated by the number inside each bar.

mitochondrial phospholipase $A_2$, which catabolizes mature cardiolipin[25]; linoleic acid (LA), an essential unsaturated fatty acid precursor of mature cardiolipin[26]; and arginine plus cysteine, amino acids that are frequently deficient in patients with BTHS[27]. LA and bromoenol lactone partially corrected the monolysocardiolipin/cardiolipin ratio in BTHS iPSC-CMs, whereas arginine plus cysteine had no effect (**Fig. 6a**). Treatment of galactose-cultured BTHS iPSC-CMs with LA or arginine plus cysteine increased ATP to levels comparable to those seen in control iPSC-CMs or BTHS iPSC-CMs rescued with *TAZ* modRNA, whereas bromoenol lactone had no significant effect (**Fig. 6b**). LA, but not arginine plus cysteine, also normalized the basal and $F_1F_0$ ATP synthase oxygen consumption rates of BTHS iPSC-CMs but had little effect on maximal mitochondrial respiratory capacity (**Fig. 6c** and **Supplementary Fig. 13**). Thus, of the three tested treatments, LA was most effective at correcting the metabolic phenotype of BTHS iPSC-CMs.

Because LA had a positive effect in each of these metabolic assays, we asked whether LA supplementation could mitigate the sarcomere organization and contractile defects of BTHS iPSC-CMs. LA improved the sarcomere organization of BTH-H iPSC-CMs (**Fig. 6d**). No statistically significant improvement was noted in BTH-C iPSC-CMs, whose sarcomeric organization was not significantly different from that of controls. In both BTH-H and BTH-C myocardial tissue constructs, LA dramatically increased twitch stress to nearly normal levels (**Fig. 6e**). This was reflected in an obvious effect of LA on rhythmic beating of the BTHS myocardial MTF constructs (**Supplementary Movie 5**). Thus, LA rescued the contractile deficits of BTHS iPSC-CMs.

In addition to potentially enhancing alternative pathways of cardiolipin synthesis, LA might also influence BTHS iPSC-CM phenotype by scavenging ROS. An extensive literature implicates high levels of ROS in ischemic and hypertensive heart failure, in part through effects on sarcomere assembly and function[28]. Uncoupling of the electron transport chain and elevated mitochondrial membrane potential, both of which were observed in BTHS iPSC-CMs (**Fig. 1** and **Supplementary Fig. 14a–d**), promote mitochondrial ROS production. Indeed, we found that mitochondrial ROS production was markedly increased in BTHS iPSC-CMs, as assessed by measurement of 4-hydroxynonenal, a product of lipid peroxidation, or as assessed by MitoSOX, a mitochondrially targeted probe with ROS-enhanced fluorescence (**Supplementary Fig. 14e**). 4-Hydroxynonenal levels were suppressed to near baseline by LA (**Fig. 6f**). To distinguish antioxidant from cardiolipin-precursor mechanisms of LA action, we tested the mitochondrially targeted and structurally unrelated antioxidant mitoTEMPO. Like LA, mitoTEMPO suppressed excessive ROS in BTHS iPSC-CMs (**Fig. 6g**).

Having confirmed that mitoTEMPO effectively suppresses excessive mitochondrial ROS in BTHS iPSC-CMs, we next determined whether mitoTEMPO treatment could improve sarcomere organization and force generation. Indeed, mitoTEMPO treatment normalized the sarcomere organization and contractility of BTHS iPSC-CMs (**Fig. 6h,i** and **Supplementary Movie 6**).

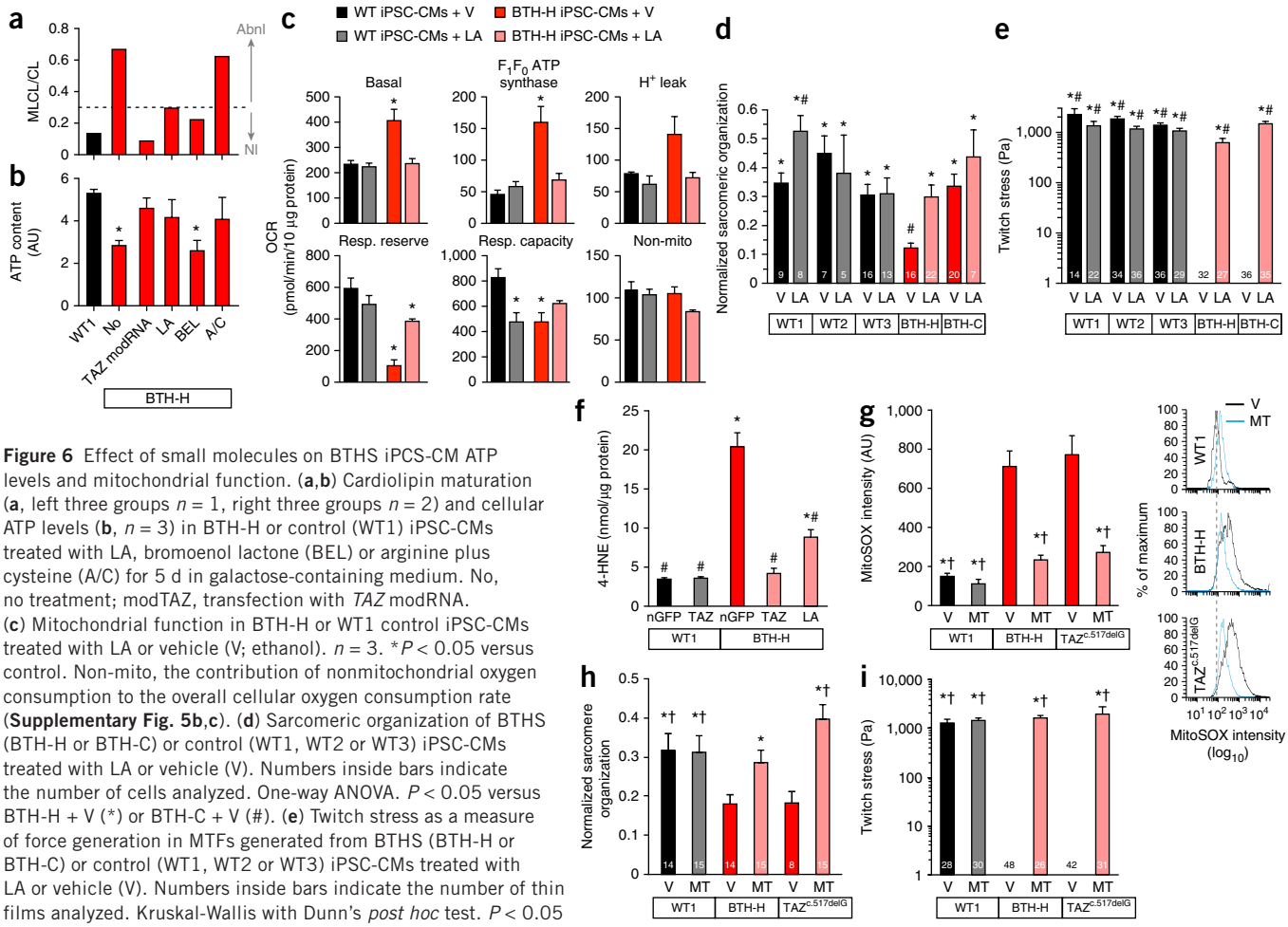


**Figure 6** Effect of small molecules on BTHS iPCS-CM ATP levels and mitochondrial function. (**a**,**b**) Cardiolipin maturation (**a**, left three groups $n = 1$, right three groups $n = 2$) and cellular ATP levels (**b**, $n = 3$) in BTH-H or control (WT1) iPSC-CMs treated with LA, bromoenol lactone (BEL) or arginine plus cysteine (A/C) for 5 d in galactose-containing medium. No, no treatment; modTAZ, transfection with *TAZ* modRNA. (**c**) Mitochondrial function in BTH-H or WT1 control iPSC-CMs treated with LA or vehicle (V; ethanol). $n = 3$. $^*P < 0.05$ versus control. Non-mito, the contribution of nonmitochondrial oxygen consumption to the overall cellular oxygen consumption rate (**Supplementary Fig. 5b**,**c**). (**d**) Sarcomeric organization of BTHS (BTH-H or BTH-C) or control (WT1, WT2 or WT3) iPSC-CMs treated with LA or vehicle (V). Numbers inside bars indicate the number of cells analyzed. One-way ANOVA. $P < 0.05$ versus BTH-H + V (*) or BTH-C + V (#). (**e**) Twitch stress as a measure of force generation in MTFs generated from BTHS (BTH-H or BTH-C) or control (WT1, WT2 or WT3) iPSC-CMs treated with LA or vehicle (V). Numbers inside bars indicate the number of thin films analyzed. Kruskal-Wallis with Dunn's *post hoc* test. $P < 0.05$ versus BTH-H + V (*) or BTHC + V (#). (**f**) Levels of the lipid peroxidation product 4-hydroxynonenal (4-HNE) in BTH-H and control (WT1) iPSC-CMs after culture in glucose and treatment with LA or the indicated modRNA for 5 d. One-way ANOVA. $n = 6$. $P < 0.05$ versus WT1 + nGFP (*) or BTH-H + nGFP (#). (**g**) Left, mitochondrial ROS as assessed by MitoSOX intensity in mitochondria isolated from BTHS (BTH-H or PGP1-TAZ$^{c.517delG}$) or control (WT1) iPSC-CMs treated with vehicle (V) or MitoTEMPO (MT). AU, arbitrary units. Right, representative histograms of three independent samples. The dashed line indicates the peak MitoSOX signal intensity from WT1 + V. One-way ANOVA. $n = 3$. $P < 0.05$ versus BTH-H + V (*) or PGP1-TAZ$^{c.517delG}$ + V (†). (**h**) Sarcomeric organization of BTHS (BTH-H or PGP1-TAZ$^{c.517delG}$) or control (WT1) iPSC-CMs plated on fibronectin rectangles and treated with vehicle (V; DMSO) or MitoTEMPO (MT). Numbers inside bars indicate the number of cells analyzed. One-way ANOVA. $P < 0.05$ versus BTH-H + V (*) or PGP1-TAZ$^{c.517delG}$ + V(†). (**i**) Twitch stress generated by MTFs assembled from BTHS (BTH-H or PGP1-TAZ$^{c.517delG}$) or control (WT1) iPSC-CMs and treated with vehicle (V) or MitoTEMPO (MT). Numbers inside bars indicate the number of thin films analyzed. Kruskal-Wallis with Dunn's *post hoc* test. $P < 0.05$ versus BTH-H + V (*) or PGP1-TAZ$^{c.517delG}$ + V(†). Data are expressed as mean ± s.e.m.

These data indicate that iPSC-CMs and heart-on-chip technology enable effective *in vitro* testing of candidate therapeutic agents. Furthermore, these data link impaired sarcomerogenesis and weak force generation in BTHS iPSC-CMs to excessive ROS production.

## DISCUSSION

Patient-derived iPSCs have considerable potential to enhance our understanding of human disease and enable therapeutic screening on a personalized basis. However, several barriers still hinder adoption of iPSC disease models academically, clinically and commercially. One obstacle to wider use of iPSC disease models has been the genetic and epigenetic variation between cell lines, which introduces confounding variables that can be difficult to control. We show that Cas9-mediated genome editing is a useful strategy to isolate a mutation of interest and show that it is sufficient to cause a disease phenotype. Gene replacement using modRNA technology is another highly portable approach that demonstrates the acute requirement of a gene mutation for a disease phenotype within a given cell line.

Another major impediment to the use of iPSCs to study human disease pathogenesis has been the lack of *in vitro* models that reproduce disease pathophysiology. With respect to cardiomyopathies, modeling the contractile function of iPSC-CMs at the level of myocardial tissue has been challenging, and prior iPSC-based models of cardiomyopathy have focused on measurements of single-cell contractile function[29,30]. Here, we assembled anisotropic laminar myocardial tissue constructs from iPSC-CMs and used these to document impaired contractile stress generation in BTHS. Furthermore, we used this approach to model phenotypic rescue at the tissue level by gene replacement and small-molecule treatments.

Our metabolic and functional analysis of human BTHS cardiomyocytes elucidated mitochondrial functional impairment caused by mature cardiolipin depletion. Our data show that the contractile

deficit of BTHS iPSC-CMs is not a result of global cellular energy depletion. Rather, we show that TAZ deficiency in BTHS impairs sarcomere assembly and contractile stress generation. It is likely that sarcomere assembly is only one of several factors that lead to reduced twitch stress in BTHS iPSC-CMs, as the extent of sarcomere disarray did not necessarily correlate with impairment of twitch stress across our assays.

We found that TAZ deficiency in BTHS caused markedly increased ROS production and that suppression of ROS normalized the metabolic, sarcomerogenesis and contractile phenotypes of BTHS iPSC-CMs. These data indicate that excessive ROS production contributes to sarcomere disarray and reduced contractile stress generation in BTHS iPSC-CMs. ROS has been implicated in cardiomyocyte differentiation, sarcomerogenesis and contractility[18,28]. Our data indicate that ROS scavenging may be beneficial for patients with BTHS and suggest that this strategy should be further validated using *in vivo* models. Our findings may be relevant to more common conditions such as ischemia and aging, as mature cardiolipin depletion and elevated ROS production also occur in these states[3].

## METHODS

Methods and any associated references are available in the online version of the paper.

*Note: Any Supplementary Information and Source Data files are available in the online version of the paper.*

### ACKNOWLEDGMENTS

This work supported by the Barth Syndrome Foundation, the Boston Children's Hospital Translational Investigator Service, the US National Institutes of Health (NIH) NHLBI Progenitor Cell Biology Consortium (NIH U01 HL100401 and U01 HL100408), NIH RC1 HL099618, NIH UH2 TR000522 and charitable donations from E. Marram, K. Carpenter and G.F. Smith.

### AUTHOR CONTRIBUTIONS

G.W. designed and performed experiments and analyzed data. M.L.M. designed and performed experiments on MTFs and sarcomere organization and analyzed data. L.Y. and G.M.C. provided expert assistance and reagents for genome editing. F.S.P. designed the sarcomere organization analysis method. H.Y. developed the MTF analysis method. A.A. assisted with MTF substrate fabrication and experiments. D.J. provided advice on mitochondrial assays. D.Z. imaged iPSC-CMs to assess their mitochondrial organization and potential. L.Z. and K.R.C. provided expert assistance with modRNA, and J.C., J.D. and D.-Z.W. helped construct modRNAs. K.L. contributed to genome editing. R.J.A.W., W.K. and F.M.V. analyzed phospholipids. M.A.L. and C.E.M. provided expert assistance in iPSC differentiation to cardiomyocytes. A.H. developed TAZ shRNA viruses and provided technical assistance. J.G. and A.E.R. obtained patient samples. Q.M. assisted in teratoma analysis. J.W. contributed control iPSC lines. R.I.K. provided expert input, patient samples and $^{31}$P nuclear magnetic resonance data. K.K.P. and W.T.P. supervised the study. W.T.P. wrote the manuscript, and it was revised by K.K.P., G.W. and M.L.M.

### COMPETING FINANCIAL INTERESTS

The authors declare competing financial interests: details are available in the online version of the paper.



1. Bione, S. *et al.* A novel X-linked gene, G4.5. is responsible for Barth syndrome. *Nat. Genet.* **12**, 385–389 (1996).
2. Houtkooper, R.H. *et al.* The enigmatic role of tafazzin in cardiolipin metabolism. *Biochim. Biophys. Acta* **1788**, 2003–2014 (2009).
3. Chicco, A.J. & Sparagna, G.C. Role of cardiolipin alterations in mitochondrial dysfunction and disease. *Am. J. Physiol. Cell Physiol.* **292**, C33–C44 (2007).
4. Karikó, K., Buckstein, M., Ni, H. & Weissman, D. Suppression of RNA recognition by Toll-like receptors: the impact of nucleoside modification and the evolutionary origin of RNA. *Immunity* **23**, 165–175 (2005).
5. Grosberg, A., Alford, P.W., McCain, M.L. & Parker, K.K. Ensembles of engineered cardiac tissues for physiological and pharmacological study: heart on a chip. *Lab Chip* **11**, 4165–4173 (2011).
6. Takahashi, K. *et al.* Induction of pluripotent stem cells from adult human fibroblasts by defined factors. *Cell* **131**, 861–872 (2007).
7. Warren, L. *et al.* Highly efficient reprogramming to pluripotency and directed differentiation of human cells with synthetic modified mRNA. *Cell Stem Cell* **7**, 618–630 (2010).
8. Warren, L., Ni, Y., Wang, J. & Guo, X. Feeder-free derivation of human induced pluripotent stem cells with messenger RNA. *Sci. Rep.* **2**, 657 (2012).
9. Shiba, Y. *et al.* Human ES-cell-derived cardiomyocytes electrically couple and suppress arrhythmias in injured hearts. *Nature* **489**, 322–325 (2012).
10. Uosaki, H. *et al.* Efficient and scalable purification of cardiomyocytes from human embryonic and induced pluripotent stem cells by VCAM1 surface expression. *PLoS ONE* **6**, e23657 (2011).
11. Elliott, D.A. *et al.* NKX2–5(eGFP/w) hESCs for isolation of human cardiac progenitors and cardiomyocytes. *Nat. Methods* **8**, 1037–1040 (2011).
12. Schlame, M. *et al.* Phospholipid abnormalities in children with Barth syndrome. *J. Am. Coll. Cardiol.* **42**, 1994–1999 (2003).
13. Kulik, W. *et al.* Bloodspot assay using HPLC-tandem mass spectrometry for detection of Barth syndrome. *Clin. Chem.* **54**, 371–378 (2008).
14. Rana, P., Anson, B., Engle, S. & Will, Y. Characterization of human-induced pluripotent stem cell-derived cardiomyocytes: bioenergetics and utilization in safety screening. *Toxicol. Sci.* **130**, 117–131 (2012).
15. Karikó, K. *et al.* Incorporation of pseudouridine into mRNA yields superior nonimmunogenic vector with increased translational capacity and biological stability. *Mol. Ther.* **16**, 1833–1840 (2008).
16. Zangi, L. *et al.* Modified mRNA directs the fate of heart progenitor cells and induces vascular regeneration after myocardial infarction. *Nat. Biotechnol.* **31**, 898–907 (2013).
17. Mali, P. *et al.* RNA-guided human genome engineering via Cas9. *Science* **339**, 823–826 (2013).
18. Hom, J.R. *et al.* The permeability transition pore controls cardiac mitochondrial maturation and myocyte differentiation. *Dev. Cell* **21**, 469–478 (2011).
19. Gerdes, A.M. & Capasso, J.M. Structural remodeling and mechanical dysfunction of cardiac myocytes in heart failure. *J. Mol. Cell. Cardiol.* **27**, 849–856 (1995).
20. Agarwal, A., Goss, J.A., Cho, A., McCain, M.L. & Parker, K.K. Microfluidic heart on a chip for higher throughput pharmacological studies. *Lab Chip* **13**, 3599–3608 (2013).
21. Feinberg, A.W. *et al.* Muscular thin films for building actuators and powering devices. *Science* **317**, 1366–1370 (2007).
22. Domian, I.J. *et al.* Generation of functional ventricular heart muscle from mouse ventricular progenitor cells. *Science* **326**, 426–429 (2009).
23. Parker, K.K., Tan, J., Chen, C.S. & Tung, L. Myofibrillar architecture in engineered cardiac myocytes. *Circ. Res.* **103**, 340–342 (2008).
24. Alford, P.W., Feinberg, A.W., Sheehy, S.P. & Parker, K.K. Biohybrid thin films for measuring contractility in engineered cardiovascular muscle. *Biomaterials* **31**, 3613–3621 (2010).
25. Malhotra, A. *et al.* Role of calcium-independent phospholipase A2 in the pathogenesis of Barth syndrome. *Proc. Natl. Acad. Sci. USA* **106**, 2337–2341 (2009).
26. Valianpour, F. *et al.* Linoleic acid supplementation of Barth syndrome fibroblasts restores cardiolipin levels: implications for treatment. *J. Lipid Res.* **44**, 560–566 (2003).
27. Rigaud, C. *et al.* Natural history of Barth syndrome: a national cohort study of 22 patients. *Orphanet J. Rare Dis.* **8**, 70 (2013).
28. Steinberg, S.F. Oxidative stress and sarcomeric proteins. *Circ. Res.* **112**, 393–405 (2013).
29. Sun, N. *et al.* Patient-specific induced pluripotent stem cells as a model for familial dilated cardiomyopathy. *Sci. Transl. Med.* **4**, 130ra47 (2012).
30. Lan, F. *et al.* Abnormal calcium handling properties underlie familial hypertrophic cardiomyopathy pathology in patient-specific induced pluripotent stem cells. *Cell Stem Cell* **12**, 101–113 (2013).

## ONLINE METHODS

**iPSC derivation and culture.** Low-passage skin fibroblasts were obtained from skin biopsies from two unrelated patients with BTHS with informed consent under protocols approved by the Boston Children's Hospital Institutional Review Board. WT1 control iPSCs were derived from BJ fibroblasts (Stemgent), and WT2 and WT3 iPSCs were described previously[7,8,31]. The BTH-H iPSC line was established by retroviral delivery of four reprogramming factors (OCT4, SOX2, KLF4 and Myc)[6]. The BTH-C iPSC line was established by modRNA reprogramming as described[7]. Several iPSC clones with embryonic stem cell morphology and with positive vital staining for TRA-1-81 or TRA-1-60 staining[32] were further characterized to yield the final two lines. Karyotyping was performed by Cell Line Genetics. Teratomas were formed by injection of $1 \times 10^6$ iPSCs intramuscularly into the flanks of adult severe combined immunodeficiency mice (Charles River Labs) under protocols approved by the Boston Children's Hospital Institutional Animal Care and Use Committee. Teratomas were examined by H&E and immunofluorescent staining. H7 human ES cells were obtained from WiCell Research Institute.

**iPSC cardiac differentiation and iPSC-CM culture.** Cardiomyocyte differentiation was induced as previously reported[9], with minor modifications. Cells were detached by 3- to 5-min incubation with Versene (Invitrogen) and seeded onto Matrigel-coated plates at a density of 10,000 cells/cm$^2$ in mouse embryonic fibroblast conditioned medium (MEF-CM) plus 4 ng/mL human basic fibroblast growth factor (Stemgent) for 2–3 d before induction. Cells were covered with Matrigel (1:60 dilution) on the day before induction. To induce cardiac differentiation, we replaced MEF-CM with RPMI+B27 medium (RPMI-1640, 2 mM L-glutamine, ×1 B27 supplement without insulin) supplemented with 100 ng/mL of Activin A (R&D Systems) for 24 h, followed by 10 ng/mL human bone morphogenetic protein-4 (R&D) and 10 ng/mL human basic fibroblast growth factor for 4 d without culture medium changes. The culture medium was subsequently replaced with RPMI+B27 supplemented with 100 ng/mL of DKK1 (R&D) for 2 d. At day 7, the culture medium was changed to RPMI+B27 without supplementary cytokines; culture medium was refreshed every 1–2 d. Leibovitz L-15 medium was substituted for RPMI for galactose-containing culture medium. For iPSC-CM enrichment, differentiation cultures were dissociated with Accumax (Innovative Cell Technologies). Dissociated cells were stained with anti–VCAM-1 antibody (**Supplementary Table 3** contains antibody information) conjugated with allophycocyanin (APC) and enriched by magnetically activated cell sorting (MACS) using anti-APC microbeads (Miltenyi Biotec). For MACS validation, sorted cells were fixed and stained with TNNT2 primary and Alexa-488–conjugated secondary antibody. Data were analyzed with FlowJo (Treestar) software. For MitoTEMPO treatment, iPSC-CMs were purified by VCAM-1 MACS and reseeded on muscle thin films at 1 million cells per well of a six-well plate (described below). The cells were treated with MitoTEMPO (Sigma) at a final concentration of 5 μM for 5 d. Linoleic acid (Sigma) was freshly prepared for each use from sealed ampules. It was dissolved in ethanol and used at a final concentration of 50 μM.

**Cas9-mediated genome editing.** Details of our modified Cas9-mediated genome editing strategy will be published separately. In brief, we constructed a piggyBac transposon that expresses the reverse tetracycline activator and a human codon–optimized Cas9 under the control of a tet response element. Stable transfection of PGP1-iPSCs (Coriell Institute for Medical Research) with this engineered transposon yielded PGP1-iPSC–hCas9 cells. We subsequently designed guide RNA and donor oligonucleotides (**Fig. 3a–c**, **Supplementary Fig. 8** and **Supplementary Table 4**) to introduce the BTH-H *TAZ* mutation into exon 6. After transient doxycycline administration and transfection with guide RNA and donor oligonucleotides, we screened individual clones by Sanger sequencing. We selected an unmodified clone, a clone containing the BTH-H mutation (resulting from homology-directed repair) and a clone containing an insertion resulting from nonhomologous end joining. Transient transfection with a plasmid expressing piggyBac transposase subsequently led to removal of the Cas9-containing transposon.

***TAZ* sequencing.** *TAZ* sequencing was performed using previously described primers[33] listed in **Supplementary Table 4**. Mutations are referenced to RefSeq NM_000116.3.

**Cardiac $^{31}$P nuclear magnetic resonance.** Cardiac $^{31}$P nuclear magnetic resonance imaging was performed as described[34] with informed consent under a protocol approved by the Institutional Review Board of the Children's Hospital of Philadelphia. High-energy phosphate stores were estimated from the phosphocreatine peak area, normalized to the peak area from the β phosphate of ATP[34].

**Mitochondrial function assays.** For mitochondrial function assays, 60,000 sorted cells were seeded in 0.1% gelatin-coated Seahorse assay wells in alpha MEM (Invitrogen) with 10% FBS. They were then changed to L-15 medium supplemented with 1x B27 supplement without insulin for 5–7 d. Oxygen consumption rate (OCR) was measured using a Seahorses Biosciences XF24 extracellular flux analyzer using the Cell Mito Stress Kit (Seahorses Biosciences) and normalized to total protein, determined using the BCA protein assay (Thermo Scientific). OCR was expressed as pmol/min/10 μg protein. Based on changes OCR after addition of FCCP, oligomycin or antimycin/rotenone, we calculated the mitochondrial function metrics described in **Supplementary Figure 5b**,**c**, as directed in the Cell Mito Stress Kit manual. For ATP assays, cells were grown in the indicated medium and supplements for 5 d. ATP assay reagent (Promega) was added directly to the wells, and light output was measured with a plate luminometer. The readout was normalized to total protein. The $F_1F_0$ ATP Synthase specific activity assay was purchased from MitoSciences and used according to the manufacturer's instructions.

**Mitochondrial isolation and FACS analysis.** Mitochondrial isolation and FACS analysis were performed to measure mitochondrial size, number, membrane potential and production of ROS. Mitochondrial isolation and FACS were performed based on described protocols[35]. In brief, iPSC-CMs were digested to single cells by Versene, and mitochondria were isolated using the Mitochondria Isolation Kit (Thermo Scientific). 20 million iPSC-CMs were pelleted by centrifugation at 850*g* for 2 min. The pellet was resuspended in 800 μl of mitochondria isolation reagent A with protease inhibitor. The suspension was vortexed at medium speed for 5 s and then incubated on ice for exactly 2 min. Next, 10 μl mitochondria isolation reagent B was added and vortexed at maximum speed for 5 s. After 5 min of incubation on ice with vortexing at maximum speed every minute, 800 μl mitochondria isolation reagent C with protease inhibitor was added. The tube was centrifuged at 700*g* for 10 min at 4 °C. The supernatant was transferred to a new microcentrifuge tube and centrifuged at 3,000*g* for 15 min. The supernatant was discarded and 500 μl mitochondria isolation reagent C was added to the pellet. The sample was then centrifuged at 12,000*g* for 5 min. The mitochondrial pellet was resuspended in 200 μl FACS buffer (Stemcell Technologies). Either MitoSOX (5 μM; Life Technologies) or TMRM (100 nM; Life Technologies) and MitoTracker green (50 nM; Life Technologies) were incubated with mitochondria at room temperature for 30 min. The sample was then analyzed by flow cytometry. Data were analyzed by using FlowJo software. Fluorescence intensity is reported in arbitrary units based on the readout of the FACS instrument.

**NRVM culture.** NRVMs were isolated from postnatal day 1 rat heart ventricles by collagenase digestion using the Neomyts isolation kit (Cellutron). Control and TAZ shRNA viruses were constructed as described previously[36] using sequences provided in **Supplementary Table 4**. NRVM isolation was performed according to protocols approved by the Boston Children's Hospital Institutional Care and Use Committee.

**Imaging and gene expression analysis.** Immunostaining for marker expression was performed using antibodies listed in **Supplementary Table 3**. Samples were fixed in 4% paraformaldehyde and permeabilized with 0.05% Triton X-100. Imaging was performed on an Olympus FV1000 or Zeiss LSM 5 LIVE confocal microscope. Quantitative RT-PCR was performed from total RNA using primers listed in **Supplementary Table 4**. SYBR green chemistry was used for real-time PCR detection on an ABI 7500 instrument. Western blotting was performed using antibodies specified in **Supplementary Table 3**.

Mitochondria were labeled using BacMam 2.0 mitochondria-RFP (Invitrogen), in which a baculovirus vector delivers RFP tagged with the mitochondrial localization sequence of pyruvate dehydrogenase E1 subunit α.

Electron microscopy was performed on a Tecnai G Spirit BioTWIN instrument. At least ten randomly selected fields containing cardiomyocytes were imaged per sample.

**Analysis of lipids.** Cardiolipin and monolysocardiolipin were analyzed by high-performance liquid chromatography-mass spectroscopy as described previously[37]. The monolysocardiolipin/cardiolipin ratio was calculated from these mass spectrum data. Lipid peroxidation product 4-HNE was measured by ELISA (Cell Biolabs).

**Modified RNA synthesis and delivery.** The iPSC reprogramming cDNA templates were obtained from Addgene[7]. The *TAZ* modRNA cDNA template was expressed from pcDNA3.3-TOPO-T7-5′UTR-cMyc-3′UTR, which contains the T7 promoter and optimized 5′ and 3′ untranslated regions (Addgene plasmid 26818)[7]. The vector was modified to place unique AscI and NheI restriction sites between the 5′ and 3′ untranslated regions. Full-length human *TAZ* cDNA corresponding to RefSeq NM_000116 with a 5′ Flag tag was cloned into the modified vector.

To synthesize modRNA, the untranslated regions and open reading frames were PCR amplified using a poly(A)-tailed primer. 1.6 µg of purified PCR product was transcribed in a 40 µl reaction system using the MEGAscript T7 kit (Ambion, Austin, TX) and a custom ribonucleoside cocktail from Allele Biotechnology (No. ABP-PP-NTPMIX) containing pseudouridine-5′-triphosphate, methylcytidine-5′-triphosphate, GTP, ATP and ARCA (Cap Analog). Reactions were incubated 6 h at 37 °C. After DNase treatment, RNA was purified with Ambion MEGAclear spin columns and then treated with Antarctic Phosphatase (New England BioLabs) for 30 min at 37 °C. Treated RNA was repurified and adjusted to a 100 ng/mL working concentration with Tris-EDTA (pH 7.0).

Modified mRNA transfection experiments were performed with RNAiMAX (Invitrogen). Transfection medium was supplemented with 200 ng/ml B18R interferon inhibitor (eBioscience). After 4 h, the transfection medium was replaced with fresh culture medium containing 200 ng/ml B18R.

**Microcontact printing.** Standard soft lithography techniques were used to fabricate polydimethylsiloxane (PDMS) stamps for microcontact printing (Sylgard 184, Dow Corning Midland, MI), as previously described[38,39]. Briefly, a silicon wafer was spin-coated with SU-8 3005 (MicroChem Corp., Newton, MA) and selectively exposed to ultraviolet light using a photomask. After being developed, the wafer was used as a template for PDMS stamps. For the single-cell studies, we used stamps with 95 µm × 13 µm rectangles. For the muscular thin film (MTF) studies, we used stamps with 15-µm wide lines separated by 2 µm.

To measure sarcomere organization in single-cell studies, glass coverslips (18 mm in diameter) were spin-coated with PDMS and cured. PDMS stamps were coated with 50 µg/mL fibronectin (BD Biosciences, San Jose, CA) for 1 h, dried and inverted onto the coverslips after treatment in a UVO cleaner (Jelight Company, Irvine, CA). Stamps were removed, and the coverslips were incubated in 1% Pluronic F-127 acid (BASF, Mount Olive, NJ) for at least 5 min before being rinsed with PBS and stored at 4 °C. MACS-purified iPSC-CMs were plated on microfabricated fibronectin islands for 5 d and transfected daily with the indicated modRNA.

**Quantitation of sarcomere organization.** For quantitation of sarcomere organization of iPSC-CMs plated on fibronectin islands, images of single myocytes stained for sarcomeric α-actinin were analyzed using custom-designed software in ImageJ (NIH, Bethesda, MD) and MATLAB (Mathworks, Natick, MA). Images were preprocessed to highlight the filamentous structure of the cytoskeleton using a tubeness operator[40], which replaces each pixel in the image with the largest nonpositive eigenvalue of the image Hessian matrix. To calculate the ability of single cells to spread across the microcontact-printed islands, the convex hulls[41] of sarcomeric α-actinin– and fibronectin-binarized immunostains were obtained and used to calculate cell projected surface area.

The regularity of spacing between the cytoskeletal elements that stained positive for sarcomeric α-actinin (**Supplementary Fig. 9a**,**b**) was assessed by first considering the magnitude of the oscillatory portion of the 2D Fourier transform of preprocessed and binarized immunostains (**Supplementary Fig. 9a**,**b**):

$$F(u,v) = \mathcal{F}\{f(x,y)\} = \iint_{R^2} f(x,y)e^{-j2\pi(ux+vy)}dxdy \quad (1)$$

To fully automate the analysis and remove any user bias[42], 512 radial profiles of the 2D Fourier transform were summed to obtain a one-dimensional representation – $\Gamma(\omega_n)$ – of the 2D spectrum (blue dots in **Supplementary Fig. 9a**,**b**) that was further normalized so that the total area under the curve would be 1. A least-square minimization was performed to find the vector of parameters $\gamma$ for which the function $\tilde{\Gamma}(\omega,\gamma)$ best fits the $N$ experimental data points:

$$\tilde{\Gamma}(\omega,\gamma) = \tilde{\Gamma}_{ap}(\omega,\gamma_{ap}) + \tilde{\Gamma}_{p}(\omega,\gamma_{p}) \quad (2)$$

$$\gamma = \min_{\gamma}\left[\sum_{n=1}^{N}(\Gamma(\omega_n) - \tilde{\Gamma}(\omega_n,\gamma))^2\right] \quad (3)$$

The functional form of $\tilde{\Gamma}(\omega,\gamma)$ was composed by an aperiodic component, representing the effect of poorly developed cytoskeletal structures (equation (4); black curves, **Supplementary Fig. 9**) and a periodic component (equation (5), red curves, **Supplementary Fig. 9**) relating to periodically spaced Z-discs:

$$\tilde{\Gamma}_{ap}(\omega,\gamma_{ap}) = a + be^{-c\omega};\ \gamma_{ap} = \{a,b,c\} \quad (4)$$

$$\tilde{\Gamma}_{p}(\omega,\gamma_{p}) = \sum_{k=1}^{5} a_k e^{-\left(\frac{\omega - k\omega_0}{\delta_k}\right)^2};\ \gamma_{p} = \{\omega_0, a_k, \delta_k\} \quad (5)$$

In agreement with Fourier analysis, the periodic component was approximated with a series of Gaussian peaks localized at integer multiples of the spatial frequency ($\omega_0 = 1/r_0$) associated with the sarcomere length ($r_0$ ~2 µm).

The area under the peaks of the periodic component was taken as a metric of structural organization and named sarcomere organization, as the organization increases as more sarcomeric α-actinin–positive elements become localized in the Z-discs at a distance ~$r_0$. We normalized all sarcomere organization values to the maximum value observed across all single cells before plotting.

**MTF fabrication and experiments.** MTF chips were fabricated on 22 mm × 22 mm glass coverslips that were 0.13–0.16 mm thick (Ted Pella, Redding, CA)[20,21]. Coverslips were covered with low-adhesion Scotch tape (3M, St. Paul, MN), and two rectangles with dimensions of 18 mm × 5.8 mm spaced 8.6 mm apart (distance from center to center) were cut into the tape with a 10.6-µm-wavelength $CO_2$ laser prototyping system (VersaLaser 2.0, 10W, Universal Laser Systems, Scottsdale, AZ). Cut rectangles were peeled using a sharp tweezer, and then a 10% (w/v) solution of poly(*N*-isopropylacrylamide) (PIPAAm, Polysciences, Warrington, PA) in 99% butanol was spin-coated at 6,000 r.p.m. for 1 min. This allowed for PIPAAm deposition within bare-glass regions. The rest of the tape was then peeled off and PDMS mixed at 10:1 ratio of base to curing agent was spin-coated at 4,000 r.p.m. for 1 min. PDMS-coated chips were placed in a 65 °C oven for at least 8 h to allow complete curing of the elastomer. The Young's modulus in compression of cured Sylgard 184 mixed in the ratio of 10:1 base/curing agent was determined to be 1.52 ± 0.05 MPa ($n$ = 18 samples, mean ± s.d.) using an Instron 3342 mechanical apparatus (Instron, Norwick, MA). In the final step, two rows of cantilever outlines were cut into the elastomer within the PIPAAm rectangular regions such that the final cantilevers were 5 mm × 2 mm or 3 mm × 2 mm, spaced 2.5 mm apart (distance from center to center)[20]. For each batch of films, the thickness of the elastomer was measured using a profilometer (Dektak 6M, Veeco Instruments, Plainview, NY) and found to be in the range of 11.4–13.4 µm.

MACS-purified iPSC-CMs were seeded on MTF constructs at a density of $1 \times 10^5$ per cm$^2$ and allowed to develop for 5 d, with daily transfection with modRNA as indicated. For contraction assays, MTF constructs were transferred to 37 °C Tyorde's buffer solution (1.8 mM $CaCl_2$, 5 mM HEPES, 1 mM $MgCl_2$, 5.4 mM KCl, 135 mM NaCl, 0.33 mM $NaH_2PO_4$ and either 5 mM glucose or galactose depending on the experimental conditions, pH 7.4) and placed on the stage of a Zeiss Discovery V8 Stereo Microscope at room temperature. Tweezers were used to manually peel each thin film away from the glass coverslip as the PIPAAm layer dissolved because of the slight drop in temperature. When




doi:10.1038/nm.3545

all films were peeled, the constructs were rewarmed to 37 °C and paced with platinum field-stimulation electrodes. Films were paced at 1, 2, 3, 4 and 5 Hz, and their movement was recorded from above at 100 frames per second. Films paced at 2 Hz were used for statistical comparison because this frequency was closest to the spontaneous beat rate.

**MTF stress quantitation.** The longitudinal planar projections of contracting MTFs were automatically detected using custom ImageJ (NIH, Bethesda, MD) software and used to calculate the radius of curvature of each film using custom MATLAB software (Mathworks, Natick, MA), as previously described[5]. The stress of the cell layer was determined from the radius of curvature using a modified form of Stoney's equation:

$$\sigma_{\text{cell}} = \frac{Et_s^2}{6(1-\nu^2)Rt_c(1+{}^{t_c}\!/_{t_s})} \quad (6)$$

where $\sigma_{\text{cell}}$ is the stress of the cell layer, $E$, $\nu$ and $t_s$ are the Young's modulus, Poisson's ratio and thickness of the PDMS film, respectively, $R$ is the MTF radius of curvature and $t_c$ is the thickness of the cell layer. Equation (6) can be readily derived based on the theory of the cylindrical bending of thin plates[43] and the static equilibrium of the force and torque of plate bending[44]. The plate modulus $E/(1-\nu^2)$ instead of the biaxial modulus $E/(1-\nu)$, appears in equation (6) because the anisotropic contraction of the cell layer bends the PDMS film into a cylindrical shape instead of a bowl-like shape. The factor $(1+t_c/t_s)^{-1}$ is a correction to the standard Stoney's equation[44] when the thickness of the cell layer approaches that of the PDMS layer. We previously used a more comprehensive model[24] to calculate not only the stress in the film but also the shortening of the muscle layer. For the MTFs used in this paper, the stresses calculated by these two methods are almost identical, so we chose to adopt the simpler analytical form of the modified Stoney's equation.

**Statistical analyses.** Results are reported as mean ± s.e.m. Unless otherwise indicated, we used unpaired Student's *t*-tests with unequal variances. Stress values failed the Shapiro-Wilkinson test for normality and were thus statistically compared using Kruskal-Wallis one-way ANOVA on ranks and Dunn's method for pairwise comparisons. Tests with a $P$ value less than 0.05 were considered statistically significant. No statistical method was used to predetermine sample size. The experiments were not randomized. The sarcomere organization and MTF assays were performed blinded to allocation during outcome assessment. Other experiments were not blinded to allocation during experiments and outcome assessment.


31. Park, I.H. *et al*. Disease-specific induced pluripotent stem cells. *Cell* **134**, 877–886 (2008).
32. Chan, E.M. *et al*. Live cell imaging distinguishes bona fide human iPS cells from partially reprogrammed cells. *Nat. Biotechnol*. **27**, 1033–1037 (2009).
33. Ichida, F. *et al*. Novel gene mutations in patients with left ventricular noncompaction or Barth syndrome. *Circulation* **103**, 1256–1263 (2001).
34. Whitman, G.J. *et al*. Diagnosis and therapeutic evaluation of a pediatric case of cardiomyopathy using phosphorus-31 nuclear magnetic resonance spectroscopy. *J. Am. Coll. Cardiol*. **5**, 745–749 (1985).
35. Chen, Y. & Dorn, G.W.n. PINK1-phosphorylated mitofusin 2 is a Parkin receptor for culling damaged mitochondria. *Science* **340**, 471–475 (2013).
36. He, A., Kong, S.W., Ma, Q. & Pu, W.T. Co-occupancy by multiple cardiac transcription factors identifies transcriptional enhancers active in heart. *Proc. Natl. Acad. Sci. USA* **108**, 5632–5637 (2011).
37. Houtkooper, R.H. *et al*. Cardiolipin and monolysocardiolipin analysis in fibroblasts, lymphocytes, and tissues using high-performance liquid chromatography-mass spectrometry as a diagnostic test for Barth syndrome. *Anal. Biochem*. **15**, 230–237 (2009).
38. Bray, M.A., Sheehy, S.P. & Parker, K.K. Sarcomere alignment is regulated by myocyte shape. *Cell Motil. Cytoskeleton* **65**, 641–651 (2008).
39. Chen, C.S., Mrksich, M., Huang, S., Whitesides, G.M. & Ingber, D.E. Geometric control of cell life and death. *Science* **276**, 1425–1428 (1997).
40. Sato, Y. *et al*. Three-dimensional multi-scale line filter for segmentation and visualization of curvilinear structures in medical images. *Med. Image Anal*. **2**, 143–168 (1998).
41. Melkman, A.A. On-line construction of the convex hull of a simple polyline. *Inf. Process. Lett*. **25**, 11–12 (1987).
42. Wei, S. *et al*. T-tubule remodeling during transition from hypertrophy to heart failure. *Circ. Res*. **107**, 520–531 (2010).
43. Timoshenko, S. & Woinowsky-Krieger, S. in *Engineering Societies Monographs* 5 (McGraw-Hill, 1959).
44. Stoney, G.G. The tension of metallic films deposited by electrolysis. *Proc. R. Soc. Lond*. **82**, 172–175 (1909).